ACS APPLIED MATERIALS & INTERFACES

Research Article

www.acsami.org

Hierarchical Hematite Nanoplatelets for Photoelectrochemical Water Splitting

Marcello Marelli,[†,‡] Alberto Naldoni,*[,†,‡] Alessandro Minguzzi,[‡] Mattia Allieta,[‡] Tersilla Virgili,[§] Guido Scavia,[∥] Sandro Recchia,[⊥] Rinaldo Psaro,[†] and Vladimiro Dal Santo*[,†]

[†]CNR−Istituto di Scienze e Tecnologie Molecolari, Via C. Golgi 19, 20133 Milano, Italy

[‡]Dipartimento di Chimica, Università degli Studi di Milano, Via Golgi 19, 20133 Milano, Italy

[§]Istituto di Fotonica e Nanotecnologie (IFN) CNR, Dipartimento di Fisica, Politecnico di Milano, 20132 Milano, Italy

[∥]CNR−Istituto per lo Studio delle Macromolecole (ISMAC), 20133 Milano, Italy

[⊥]Dipartimento di Scienza e Alte Tecnologie, Università dell'Insubria, 22100 Como, Italy

Supporting Information

ABSTRACT: A new nanostructured α-Fe_2O_3 photoelectrode synthesized through plasma-enhanced chemical vapor deposition (PE-CVD) is presented. The α-Fe_2O_3 films consist of nanoplatelets with (001) crystallographic planes strongly oriented perpendicular to the conductive glass surface. This hematite morphology was never obtained before and is strictly linked to the method being used for its production. Structural, electronic, and photocurrent measurements are employed to disclose the nanoscale features of the photoanodes and their relationships with the generated photocurrent. α-Fe_2O_3 films have a hierarchical morphology consisting of nanobranches (width ∼10 nm, length ∼50 nm) that self-organize in plume-like nanoplatelets (350−700 nm in length). The amount of precursor used in the PE-CVD process mainly affects the nanoplatelets dimension, the platelets density, the roughness, and the photoelectrochemical (PEC) activity. The highest photocurrent (j = 1.39 mA/cm^2 at 1.55 V_{RHE}) is shown by the photoanodes with the best balance between the platelets density and roughness. The so obtained hematite hierarchical morphology assures good photocurrent performance and appears to be an ideal platform for the construction of customized multilayer architecture for PEC water splitting.

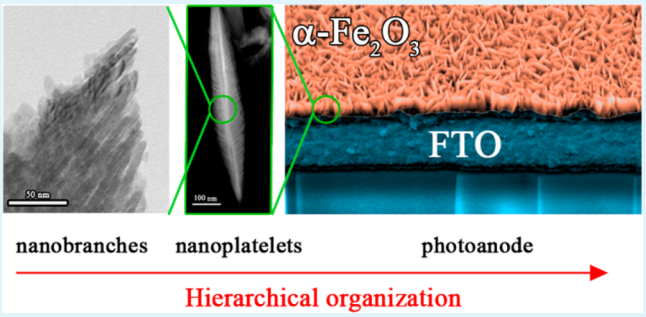

KEYWORDS: *hierarchical structures, hematite, photocatalysis, water splitting, solar fuels*

INTRODUCTION

The development of enabling technologies to efficiently harvest and use solar energy is one of the main challenges of our society. The utilization of inorganic semiconductors in photoelectrochemical (PEC) water splitting is an ideal approach to yield highly pure hydrogen, a versatile energy vector that can be converted either to methane (by the Sabatier process, with the additional advantage of CO_2 fixation) or to electrical power by fuel cells. To maximize the utilization of the solar spectrum, many efforts have been made to develop efficient visible light absorbers, such as hematite (α-Fe_2O_3), $BiVO_4$, InP, TaON, Ta_3N_5, and Cu_2O.[1−3]

Among all candidates, α-Fe_2O_3 is considered the prototypical material because: (i) it is a simple oxide with a favorable bandgap (ca. 2.1 eV); (ii) it is highly stable under PEC condition, and (iii) it is made of abundant elements.[4−7] On the other hand, the engineering of the physicochemical properties of α-Fe_2O_3 is crucial to optimize its poor hole diffusion length (2−4 nm), low light penetration depth (α^{-1} = 118 nm at λ = 550 nm), electrolyte diffusion, and electrocatalyst deposition.[8] In addition, high doping level by means of aliovalent elements (i.e., Sn^{4+}) is required to obtain α-Fe_2O_3 with significant PEC activity.[8−10] Sn^{4+} doping results in a thin space-charge layer (SCL), thus being the majority of the photons absorbed far from it and reducing the chance that photogenerated holes reach the semiconductor-electrolyte junction. However, the SCL to bulk ratio can be maximized by nanoscale engineering, reducing recombination and increasing the plateau current.[9] For instance, nanoparticle films have shown high PEC activity because of their small size (i.e., 10 nm).[9−12] Low-dimensional and nanostructured materials are appealing alternatives. Representative examples include α-Fe_2O_3 nanosheets,[13,14] oriented array of nanorods/hexapods,[15,16] arrays of nanotubes,[17] nanowires,[18−20] and nanocorals.[21]

State of the art doped α-Fe_2O_3 shows photocurrent at 1.23 V_{RHE} ranging from 1.26 mA/cm^2 (Sn-doped nanorods[16]) to 1.8 mA/cm^2 (Si-doped cauliflower-type structure[9]). Significant improvement in photocurrent response can be obtained

Received: January 30, 2014
Accepted: July 9, 2014
Published: July 9, 2014

through noble metal codoping and surface modification with electrocatalyst and/or passivation layer.[9,16] The outstanding performance of 4.32 mA/cm^2 (34% of maximum theoretical limit for α-Fe_2O_3) has been obtained with Sn−Pt codoped α-Fe_2O_3 nanorods modified with a Co−Pi surface layer.[16]

Here, we present a α-Fe_2O_3 with a new hierarchical morphology obtained through PE-CVD synthesis. Such nanostructure consists of aligned nanobranches that self-organize in plumelike nanoplatelets composed by α-Fe_2O_3 crystalline phase with (001) planes being perpendicular to FTO substrates. The structural and electronic properties of α-Fe_2O_3 films were characterized by XRD, SEM, AFM, HRTEM, STEM-HAADF, UV−vis, and ultrafast pump−probe spectroscopy. PEC tests revealed that α-Fe_2O_3 plumelike hierarchical nanoplatelet is a promising morphology for efficient PEC water splitting, showing a photocurrent of 1.39 mA/cm^2 at 1.55 V_{RHE}.

EXPERIMENTAL SECTION

PE-CVD Growth of α-Fe_2O_3 Photoanodes. The α-Fe_2O_3 photoanodes were grown on conductive FTO coated glass slides (Aldrich) of 13 × 13 mm. The substrates were cleaned by sonication in deionized Milli-Q-Water (Millipore Corp., 18.2 MΩ cm at 25 °C), ethanol and acetone (10 min for each step). The α-Fe_2O_3 platelets were synthesized by using PE-CVD: the scheme and a detailed description of the apparatus is reported in Figure S1 (see the Supporting Information). Briefly, the organometallic precursor (ferrocene) vapors were injected axially by a pulsed Ar flow (100 mL/min at 6 Hz) into the core of a cold tubular plasma (power 30 W, RF of 13.56 MHz) fed by an Ar/O_2 4.5% gas mixture. The FTO target was placed orthogonally with respect to the gas flow, plunged in the plasma plume at 5 cm from the core. Different amounts of precursor were used: 1, 2, 3, and 5 mg of ferrocene were sublimated on sample H1, H2, H3, and H5, respectively. Prior to PEC tests, all photoelectrodes were subjected to a two-step thermal cycle including 1 h at 500 °C and 10 min at 750 °C (providing doping by Sn^{4+} diffusion from FTO),[10] followed by fast cooling at room temperature.

Characterizations. X-ray diffraction (XRD) patterns were recorded in the $20° \leq 2\theta \leq 70°$ range employing the Cu−Kα radiation at room temperature. Diffraction data were collected by placing directly the FTO film within the sample holder of the diffractometer. Rietveld analysis was performed using the GSAS software suite of programs.[22] Structural models for SnO_2 and α-Fe_2O_3 phase were taken from references.[23,24] The background was subtracted using the shifted Chebyshev polynomials and the diffraction peak profiles were fitted with a modified pseudo-Voigt function. The generalized spherical harmonic (GSH) model implemented in GSAS was used to account for the preferential orientation contribution to the diffracted intensities. Goal of our Rietveld analysis was to determine the accurate d-spacing values for the crystalline α-Fe_2O_3 phase by accounting for the diffractometer zero point correction together with GSH model. In particular, the nearly complete extinction of (hkl) with $l \neq 0$ peaks in almost all the patterns does not allow an accurate determination of the c-axis length and, hence, of the unit cell. For this reason, only the d-spacing values related to the statistical significant diffraction peaks are discussed throughout.

UV−vis measurements of α-Fe_2O_3 photoanodes were recorded with a Thermo Scientific Evolution 600 spectrophotometer using FTO glass as reference.

The morphology of films was characterized through a XL30 environmental scanning electron microscopy (ESEM-FEG Philips) under high vacuum and/or low pressure condition at 20 keV.

The HRTEM/STEM analysis were carried out by using a ZEISS LIBRA 200FE HR-TEM at 200 keV with an analytical double tilt probe ($\alpha \pm 30°$; $\beta \pm 15°$). Scanning transmission electron microscopy (STEM) micrographs were collected by a high angular annular dark field (HAADF) detector. Specimen were prepared by gentle scratching the α-Fe_2O_3 film on the substrates and collecting the small platelets by adherence to a holey carbon-coated copper TEM grid.[25]

AFM measurements were performed with a commercial AFM (NTMDT-NTEGRA) in semicontact/tapping mode with cantilevers having typical resonance frequency 87−230 kHz, force constant 1,45−15,1 N/m.

The ultrafast pump−probe (P&P) apparatus consisted of a Ti:Sapphire laser with grating-assisted chirped-pulses amplification, that delivered pulses at 780 nm with 1 kHz repetition rate. The beam is then split in two beams, the pump and the probe. This last was focused on a sapphire plate for the white light continuum (WLC) generation (470−770 nm). The pump beam was focused on a beta-barium borate (BBO) crystal for the second harmonic generation (390 nm, E_{pump} = 900 nJ). On the pump line, a delay stage controlled the temporal delay between the pump and the probe. Both beams were then focused in the sample. The pump circular spot on the sample has a radius of around 75 μm. The transmission of the probe through the sample was collected, sent in a monochromator and then on a photodiode array. The collected signal was the differential transmission spectra $\Delta T/T(\lambda,t)$ of the probe through the sample.[26]

Photoelectrochemical Measurements. PEC measurements were conducted in 1 M NaOH (pH 13.6) by using a three-electrodes cell configuration, with the α-Fe_2O_3 photoanode as the working electrode, an Ag/AgCl reference electrode, and a Pt coil as the counter electrode. Photocurrent density was measured under front-side illumination with the photoanodes located 5 mm from the cell wall, thus minimizing the light optical path across the electrolyte solution. The light source was 1 sun (AM 1.5G) solar simulator (Lot Quantum Design LS0306) equipped with a tunable 150−300 W xenon arc lamp and an Oriel AM 1.5 filter. The potential scan rate was 20 mV/s.

The IrO_x cocatalyst was prepared following the procedure reported elsewhere.[27] The protocol lead to the formation of a yellow solution, which turned into blue/violet after 3 days at room temperature. The blue colloid was used as a deposition bath, from which IrO_x was easily deposited onto the α-Fe_2O_3 film by applying 0.1 mA cm^{-2} for 600 s, using a Pt plate as the counter electrode.

RESULTS

Figure 1 shows SEM images of H1, H2, H3, and H5 samples, obtained by using 1, 2, 3, and 5 mg of ferrocene. All photoanodes showed a nanostructured morphology composed of platelets growing perpendicular to the FTO-coated glass slides (Figure 1 and Figures S3 and S4 in the Supporting Information). The width of such nanostructures was on the order of the tens of nanometers. Statistic counting based on the SEM images, instead, revealed that the length of the nanoplatelets was 357 ± 68 nm for H1, 376 ± 93 nm for H2, 425 ± 139 nm for H3, and 683 ± 207 nm for H5. The ferrocene loading affected the size distribution (see Figure S5 in the Supporting Information), which became broader at higher value passing from H1 to H5. Conversely, the platelets density, followed the order H2 (102 platelets/μm^2) > H1 (85 platelets/μm^2) > H3 (65 platelets/μm^2) > H5 (34 platelets/μm^2). This indicates that the H2 sample contained the highest number of platelets, whereas when increasing the precursor loading from H1 to H5, less dense films were formed in view of the larger platelets size (H3 and H5).

Figure 2a shows the XRD patterns of synthesized photoanodes. Most of the diffraction peaks can be assigned to SnO_2 (cassiterite phase, space group $P4_2/mnm$) related to the FTO coating of the glass substrate. By taking the diffraction pattern for powdered α-Fe_2O_3 sample as a reference (see Figure S6 in the Supporting Information), only two strong peaks due to α-Fe_2O_3 with (110) and (300) indexes were present in our patterns, suggesting strong preferential orientation (PO) of crystallographic planes.[10,28]

To follow the evolution of (110), (300) with the increasing ferrocene amount, in Figure 2b we plotted the ratio (R)

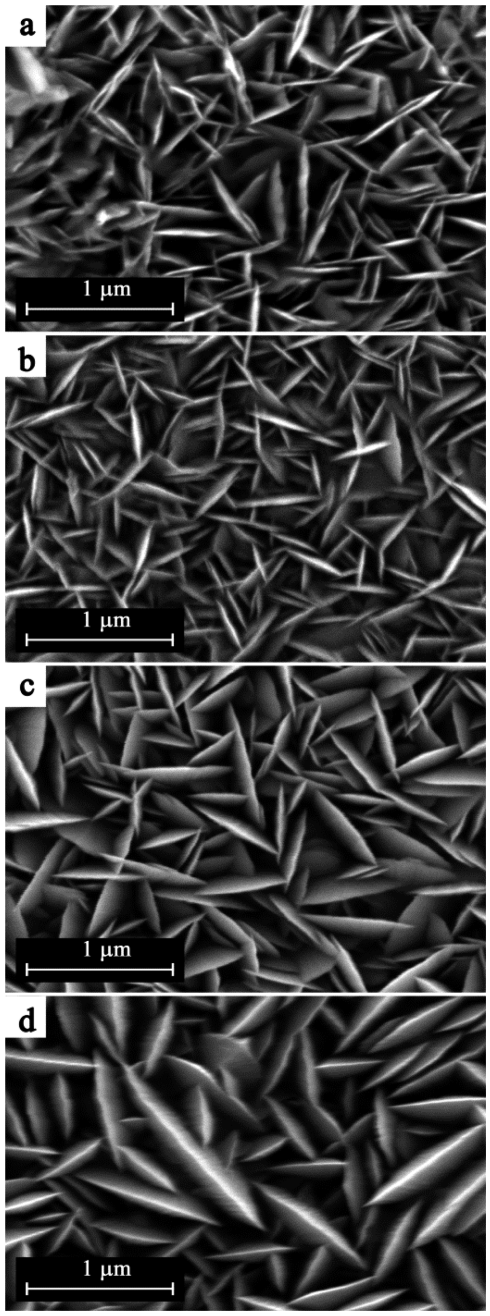

Figure 1. SEM micrographs at 30 kX magnification of all hematite films: (a) H1, (b) H2, (c) H3, (d) H5.

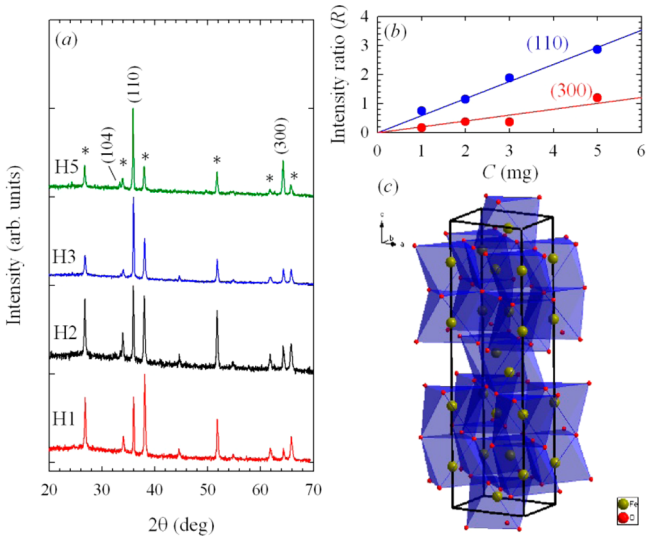

Figure 2. (a) XRD patterns of all hematite films. Miller index indicate peaks related to α-Fe_2O_3 diffraction. Asterisks indicate the diffraction peaks related to the FTO substrate. The peak around 45° 2θ is due to the sample holder. (b) Intensity ratio (R) as a function of amount of precursor (C) plotted using the equation $R = aC$. (c) Representation of α-Fe_2O_3 unit cell. Arrangement of irons form pairs of octahedra sharing edges with three neighboring octahedral within the same (001) plane and one face with an octahedron in an adjacent plane along the c-axis.

between the α-Fe_2O_3 reflection intensities and the (200) peak intensity belonging to SnO_2 phase (glass substrate) against the amount of iron precursor employed (C). It is evident that passing from H1 to H5 samples both intensities of α-Fe_2O_3 gained intensity with respect to SnO_2 scattering. A linear dependence, $R = aC$, where a is the slope of the interpolating line, was found for both the (110) and (300) intensities. This suggests a linear growth of α-Fe_2O_3 layer thickness on the FTO surface with increasing of the amount of precursor used in the PE-CVD process.

The crystallite size parameter (D_v) was determined from the broadening of XRD peaks. In α-Fe_2O_3 nanostructured films, this parameter can be related to the average length of coherent structure domains. Estimated D_v values ranging from ~30 to 50 nm (see Table S1 in the Supporting Infomration) are in agreement with the nanobranches length (~50 nm) as observed in STEM images (see Figures S8 and S10 in the Supporting Information).

d-Spacing values related to (110) and (300) peaks are reported in Figure S7 in the Supporting Information for all the samples. In the same figure, the value obtained from a powdered α-Fe_2O_3 sample are also shown as a reference. Interplanar distances decreased with increasing of precursor amount. Conversely, with respect to powder sample, an expansion was observed in all the samples. Similar relaxation of α-Fe_2O_3 structure has been already observed in hematite film and it was ascribed to the incorporation of Sn ions in the hematite lattice.[8] In our case, we obtained d-spacing expansion from 0.23% for H1 to 0.09% for H5, which is consistent with the small size difference between Sn^{4+} (0.69 Å) and Fe^{3+} (0.65 Å).[8]

To have deeper insights into both the morphology and structure of our platelets photoanodes, we used a combination of TEM, STEM, and AFM measurements.

Images a and b in Figure 3 show isolated nanoplatelets scratched from the α-Fe_2O_3 film H2 and collected on the TEM grid. Their dimension is in the range of hundreds of nanometres, in agreement with SEM statistic counting. The high-resolution micrograph (Figure 3b) shows the high crystallinity of the sample H2. Local fast Fourier analysis indicates a single crystal-like structure showing the (0−14) reflection characterized by the interplanar distance d = 0.265 nm. Because the nanoplatelets grow along the [110] direction, Figure 3 represents the structural top view. The HAADF-STEM image, shown in Figure 3c, highlights the presence of organized plumelike structures. Thus, the α-Fe_2O_3 photoanodes have two levels of hierarchical organization on multiple length scales: the smallest building blocks (tens of nm) assemble in the nanoplatelets (hundreds of nm) that constitute the nanofeatured film. Importantly, this morphology was

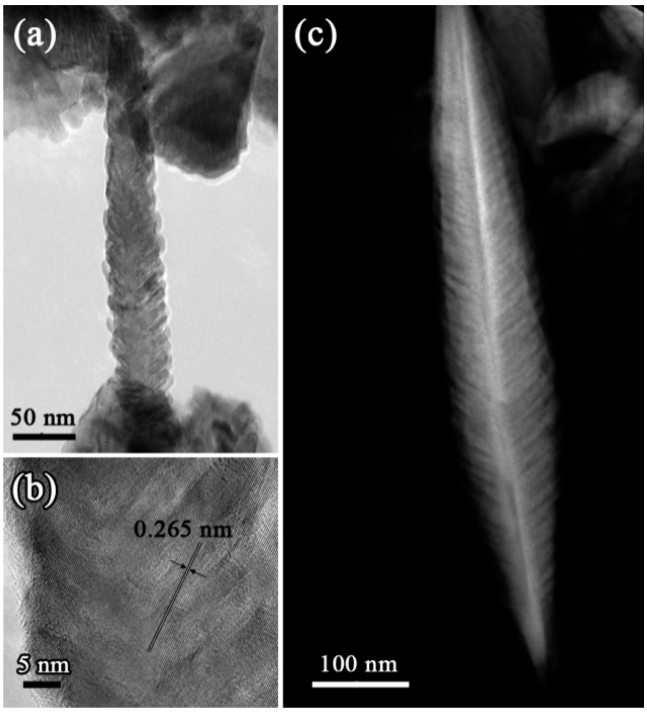

Figure 3. TEM image of isolated platelets forming the H2 film. (a) Full overview and (b) relative high-resolution micrograph of a crystalline hematite platelet. (c) HAADF-STEM micrograph representing the hierarchical morphology of the hematite platelets.

retained along with the ferrocene loadings (Figure 1 and Figure S8 in the Supporting Information).The AFM measurements (Figure 4) confirmed the main structure already revealed by SEM and disclosed the fine arrangements of the hierarchical organization (Figure 4b, c). In addition, AFM images enabled us to extract the root-mean-square (rms) roughness of investigated α-Fe_2O_3 films, which is an interesting parameter that could be related to the water splitting activity. The roughness increased in the order H1 (25.9 nm), H2 (46.4 nm), H3 (64.6 nm), accordingly to the ferrocene loading. Conversely, H5 did not follow this trend showing RF equal to 32.3 nm.

UV−vis spectra of synthesized photoanodes (see Figure S9 in the Supporting Information) show that the threshold absorption is located around 600 nm for all samples. The intensity and the background absorption increase monotonically with the increase in the amount of ferrocene used.

The time-dependent dynamics of photogenerated charges was further studied by ultrafast P&P spectroscopy. Figure 5

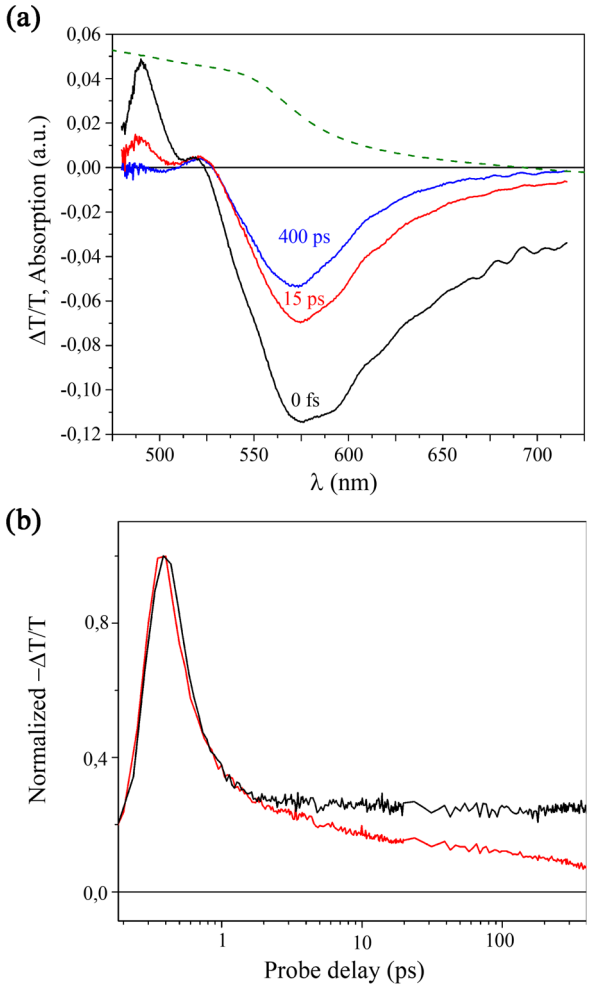

Figure 5. (a) Differential transmission spectra of the H2 sample taken at different probe delays. Dashed line represents the normalized absorption spectrum. (b) Normalized temporal decays at 540 nm (black line) and at 650 nm (red line).

represents the $\Delta T/T$ spectra at different probe delays for the as-synthesized H2 sample. By comparison with the absorption

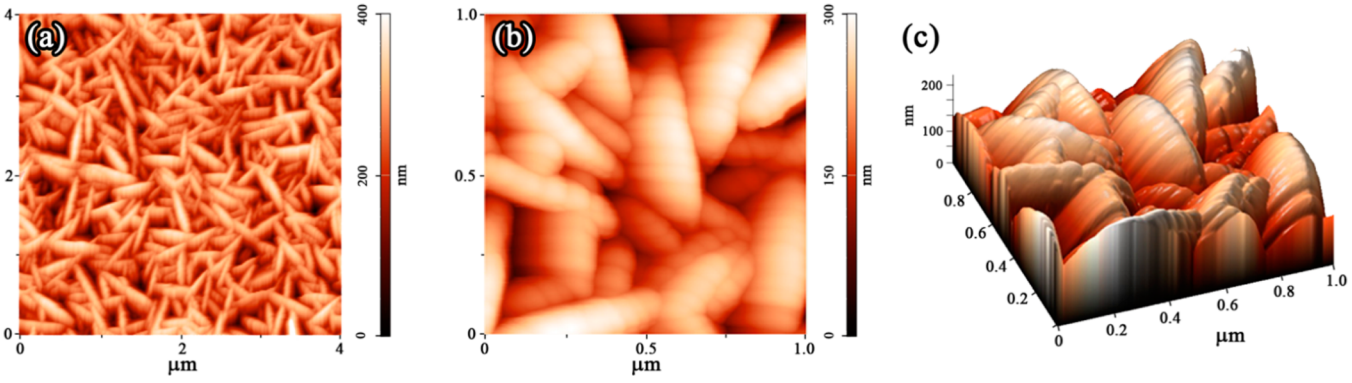

Figure 4. AFM measurements in height mode: (a) overview, (b) detail, and (c) relative 3D reconstruction of the H2 film. The platelets nanostructured features are clearly visible.

dx.doi.org/10.1021/am5030287 | ACS Appl. Mater. Interfaces 2014, 6, 11997−12004

spectrum (green dashed line) we can attribute the positive signal in the blue region of the spectrum to the bleaching of the ground state, whereas the negative region peaked at around 580 nm to the presence of a photoinduced absorption band (PIA) because of the presence of charged states.[29]

The photocurrent−voltage (j−V) characteristics of all α-Fe_2O_3 photoanodes are reported in Figure 6a. The dark current

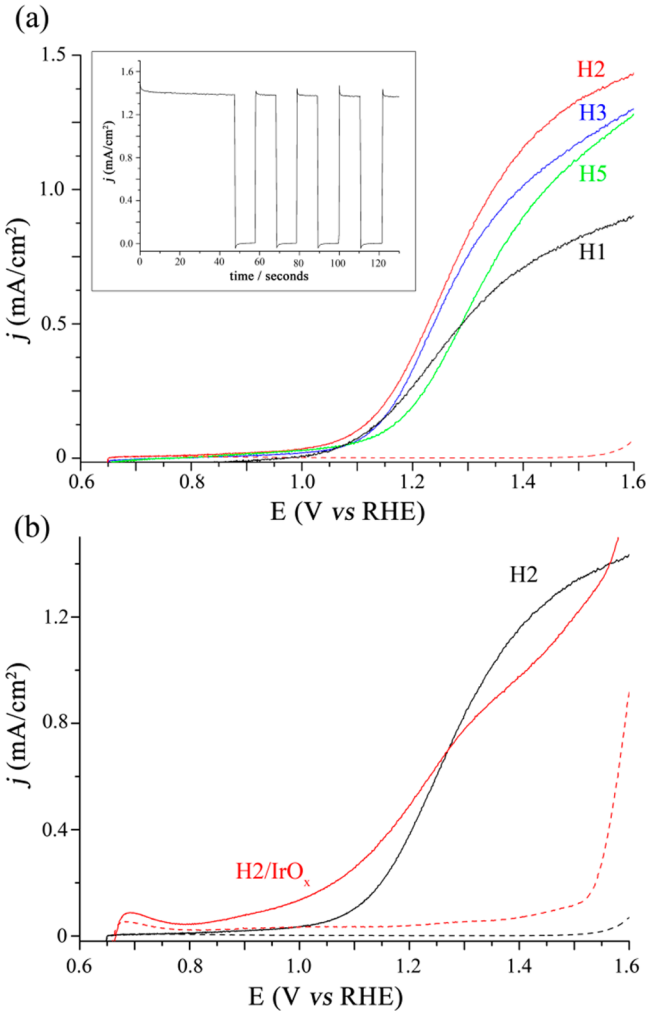

Figure 6. (a) Photoelectrochemical response of hematite electrodes showing the photocurrent (solid lines) for H1 (black), H2 (red), H3 (blue), and H5 (green). The dark current for all samples shows comparable values so we report only the curve for H1 (red dashed line).The inset shows the cronoamperometry of H2 at an applied potential of +1.6 V versus RHE under light-chopping conditions (AM 1.5G 100 mW/cm^2). (b) Photocurrent density of H2 photoanode without (black solid line), with deposited IrO_x cocatalyst (red solid line), and related dark currents (black and red dashed lines, respectively).

for all samples was 2 orders of magnitude lower than when the photoelectrodes were illuminated. The H2 photoanode showed the highest j at both the chosen reference applied bias (see Table S2 in the Supporting Information). In particular, H2 showed j = 0.53 mA/cm^2 at 1.23 V_{RHE} and j = 1.39 mA/cm^2 at 1.55 V_{RHE}. The cronoamperometry (Figure 6a, inset) measured on the H2 film at an applied potential of +1.6 V_{RHE} showed just a slight reduction in photocurrent over more than 200 s indicating the good stability of the photoelectrode. On the H2 sample (i.e., the most promising one), we have deposited IrO_x catalyst for the oxygen evolution reaction as a preliminary attempt to increase the photoelectrode photoefficiency. The deposition of IrO_x nanoparticles onto the surface of H2 induced beneficial effect in the photocurrent (Figure 6b) until the applied voltage remained lower than ∼1.3 V. Specifically, the activity enhancement was more marked at 1.0 and 1.1 V applied bias where the photocurrent raised from 0.035 and 0.103 mA/cm^2 without cocatalyst, to 0.135 and 0.257 mA/cm^2 in the presence of IrO_x, respectively.

DISCUSSION

One of the attractiveness of our plasma experimental apparatus is its flexibility that allowed us to easily span from the condition of chemical vapor condensation (CVC) synthesis to PE-CVD. By analyzing the material accumulated on the filter downstream the deposition unit (CVC mode, distance from plasma core >10 cm, outside the plasma region), we observed nanoparticles with diameter of 10 nm that pile-up into PEC not active compact films. Conversely, when the FTO target was plunged inside the plasma plume (PE-CVD mode) ordered nanostructured systems were obtained, without any presence of nanoparticles originated by parasitic CVC processes. Intermediate distance gave hybrid structures (nanoparticles/nanoplatelets, see Figure S2 in the Supporting Information), resulting again in poor PEC activity. Differently, when the target distance was fixed at 5 cm from the plasma core, the resulting morphology was characterized by a single nanoplatelet layer (see SEM cross-section, Figure S3 in the Supporting Information).

Because of that, we tuned the structure by varying only the loading of iron precursor, keeping constant all the other parameters (gas flow, sublimation temperature, target position, RF power). The increase of precursor used in the PE-CVD did not affect the main morphology of the films building blocks, but resulted in the growth of α-Fe_2O_3 film composed by nanoplatelets with higher length and a broader size distribution (Figure 1 and Figures S4 and S5 in the Supporting Information). This influenced the platelets density and the film roughness. The highest density was obtained for H2 (102 platelets/μm^2), whereas the increase in precursor loading induced a less dense film in view of the larger platelets size (H5 = 34 platelets/μm^2). The platelet density and size affected the roughness of the investigated films: H2 and H3 showed the highest values, whereaes H1 and H5 presented the lowest ones. The roughness is an important parameter that give indication on the semiconductor/water interface and its influence on PEC activity is discussed in the next paragraphs.

Interestingly, the nanostructured photoanodes were already highly crystalline after the PE-CVD without any further thermal treatment. After the ferrocene was decomposed by the nonequilibrium cold plasma, the kinetic energy of plasma electrons ($T_e \approx 1 \times 10^5$ K)[30] was transferred to the growing iron oxide film that crystallizes in situ forming nanoplatelets composed by crystalline α-Fe_2O_3.

Figure S6 in the Supporting Information shows the diffraction patterns for H5 sample and α-Fe_2O_3 powdered samples. By taking this latter pattern indexing as a reference, it is evident that there are only two strong peaks due to α-Fe_2O_3 in H5 sample with (110) and (300) indexes.

Similar strong (110) diffraction was also observed for α-Fe_2O_3 nanowires and nanobelts grown by thermal oxidation[26] or vapor deposition techniques.[10] In these studies the

dx.doi.org/10.1021/am5030287 | ACS Appl. Mater. Interfaces 2014, 6, 11997−12004

prevalence of the (110) intensity was reported as a clear indication of a strong PO of the [110] direction, which was assumed to be normal with respect to the substrate. However, even a simple crystallographic justification of such orientation is still lacking in all these studies, and besides, the PO effect related to other family of planes, like (300), is not considered to evaluate the orientation of nanocrystals. In the following, we try to elucidate it by providing an argument to derive the orientation of crystallographic planes of α-Fe_2O_3 with respect to FTO film for H5 sample taken as an example.

It should be noted that in our experimental setup the diffraction data were collected in reflection mode by placing the deposited FTO samples parallel to the sample holder. Dealing with this geometry, the crystallographic planes parallel to the FTO surface were those that contribute mainly to the diffracted intensities. By comparing the Miller index of α-Fe_2O_3 in powder and H5 samples (see Figure S6 in the Supporting Information), it is clear that within the background intensity of the pattern, (hkl) peaks with $l \neq 0$ showed partial or complete extinction. Conversely, the family of lattice planes (110), (300) which diffracted the beam, i.e., family of lattice planes parallel to the FTO surface, were those that did not intersect the z-axis. Taking the z-axis parallel to the FTO surface, within the hexagonal crystal system, the directions perpendicular to (110) and (300) planes were [110] and [210], respectively. To find the plane containing [110], [210] directions, we took the vector product, which gives the family of planes (001). From this straightforward argument, we show that the PO of the (001) planes perpendicular to the FTO surface gave rise to the observed H5 diffraction patterns. In this context, we can distinguish between two cases: (1) if only the (110) peak is observed in the pattern, the [110] direction coincides with the nanocrystals growth direction perpendicular to FTO surface; (2) if only the (300) peak is observed, the [210] corresponds to the direction of crystals growth normal to the FTO surface. Intermediate cases involving the prevalence of both peak intensities can suggest a nontrivial nanocrystals orientation involving bending or modulation of α-Fe_2O_3 arrays.[10] We point out that in these situations is more convenient to link the PO effect only to (001) family of planes instead of crystal growth direction.

The electron conduction pathways in our system were enhanced due to the strong PO of the (001) plane perpendicular to the FTO substrate observed in our films that could facilitate the collection of photogenerated electrons. At the same time, photogenerated holes could travel toward the α-Fe_2O_3/electrolyte interface by hopping between parallel (001) planes promoting the water splitting to produce molecular oxygen. Actually, the hematite structure is based on the hexagonal close packed (hcp) arrangement of O^{2-} anions. Fe^{3+} cations occupy the two-thirds of the octahedral sites in the (001) planes (Figure 2c). In this structural view, layers of close packed O^{2-} anions alternate with iron layers along the c-axis, and electrons can be delocalized by hopping through Fe^{2+}/Fe^{3+} valence states only within the iron layers, giving rise to an anisotropic conductivity four times more efficiently within the (001) plane.[10] Nevertheless, the alignment of α-Fe_2O_3's highly mobility planes perpendicular to the substrate is not the only structural property that affects its PEC efficiency. The role played by the semiconductor's nanostructuring is crucial to optimize the SCL with respect to that of the bulk and thus enhancing the electrode plateau current.

The nanostructured α-Fe_2O_3 photoanodes synthesized through our customized PE-CVD apparatus had novel structure and morphology too. The characterizations reported here shed light on the structural organization of the film, which was based on two levels of hierarchical growth. The smallest building blocks (i.e., nanobranches, 10 nm thick and 50 nm long grown parallel one to each other assembling in nanostructured platelets. The hierarchical nature allows one, in principle, to optimize separately the materials charge transport properties by engineering the features of the two levels of structural organization. For example, the control on nanobranches' growth is crucial for determining the dimensions of these building blocks (e.g., a width in the range of 10−20 nm can be considered a good target value considering the short hole diffusion length in α-Fe_2O_3), and their reciprocal spacing. On the other hand, the dimension of nanoplatelets accumulated at the FTO surface dictated both the platelets density and thickness of the film. Nevertheless, addressing the exact direction and pathway of photogenerated charges in our nanoplatelets is not trivial and it will the subject of a dedicated study.

The time-resolved optical properties of the H2 photoelectrodes (i.e., the most active) were studied through a P&P experiment, which showed the initial creation of charged states after light excitation. The optoelectronic efficiency of any material is strongly linked to the charges generation in the first picoseconds after excitation. In the $\Delta T/T$ spectra of the H2 photoelectrode (Figure 5), the PIA band due to charged states was instantaneously created. It is interesting to note that this band in time presented a blue shift and a narrowing. This effect was theoretically postulated by Cherepy et al.[31] and for the first time experimentally observed in our samples. This behavior could indicate an initial presence of electrons in the conduction band or in shallow traps, absorbing in the red-IR probe range, and then a subsequent quickly decay to deep traps more localized or midgap states with a smaller absorption cross section. If this happened we should see a faster relaxation time for redder probe wavelengths than for the blue ones. Indeed this is shown in Figure 5b, where the dynamics at 540 and 650 nm are shown. The fast decay component was present in both wavelengths, conversely, the slow one was present just in the blue part of the visible spectrum. This is a clear indication that after light excitation we create an electron populations, which in time get trapped deeply in midgap states. Probably this is the charges population responsible for the photocurrent reported in the PEC measurements.

The photocurrent densities (j) for all photoelectrodes are plotted against the potential vs RHE and displayed in Figure 6a. The photocurrent at 1.23 V_{RHE} (Table S2) steadily increased as the precursor loading increased from H1 (0.37 mA/cm^2) to H2 (0.53 mA/cm^2) (H3 shows similar activity to H2, namely, 0.48 mA/cm^2), after which further increase of the loading resulted in the reduction of photocurrent density (j_H5 = 0.29 mA/cm^2). The best activity was obtained for H2 (and H3), while H1 and H5 presented the lowest responses. This behavior can be rationalized by taking in account the film morphology features extracted by SEM and AFM images. Both roughness and platelets density crucially influenced the photocurrent response of tested photoanodes. For examples, H2 and H3 showed the best balance between the two morphological parameters thus leading to the most performing samples. In addition, the poor activity of H1 film can be also ascribed to the amount of α-Fe_2O_3 deposited on FTO, the thickness was too low to

optimize the light absorption. On the other hand, the photoactivity of H5 was further influenced by the formation of addition nanoparticles on the top of the nanobranches. The HRTEM of H5 (see Figure S10a, b in the Supporting Information) shows that at few extremities of the nanobranches, α-Fe_2O_3 crystals with different crystallographic orientation (see Figure S10c, d in the Supporting Information) have grown. Using their cauliflower-like morphology, Grätzel and co-workers[11] have recently pointed out the importance of grain boundaries in α-Fe_2O_3 photoanodes. They suggested that there are champion nanoparticle aggregates with similar crystallographic orientation that might have photon-to-current efficiency approaching the theoretical limit. Otherwise, the thermionic emission across the high angle boundaries (an interface misorientation greater than 15°) reduces the generated photocurrent by hindering the electrons percolation pathway.[11] We think that this observation can be extended to our H5 photoanode. Our nanobranches/nanoparticles interface can be classified as a high angle boundary since the angle mismatch between the two orientations is ∼43° as reported in the FFT images in Figure S10c, d in the Supporting Inforamtion (nanobranches show reflections of (0−14) plane, whereas the nanoparticles' ones belong to the (−102) plane).

H2 photocurrent (0.53 mA/cm^2) was ca. 42% of the PEC activity measured for the outstanding α-Fe_2O_3 photoanode.[16] H2 were further improved by the deposition of IrO_x cocatalyst. IrO_x is one of the most active material toward the oxygen evolution reaction (OER) in the whole range of pH.[32] Long-time experiments clearly demonstrated the instability of IrO_2 nanoparticles in alkaline solutions under intense production of oxygen.[9] However, the use of IrO_x catalyst was possible provided if applied potential was kept below 1.8 V (RHE) and working time was limited to few hours.[32] Here we toke advantage of a well-established procedure that led to electrodeposited highly hydrated iridium oxide films. This method produced reproducible amorphous films (TEM did not displayed nanoparticles as in ref 33) easily and rapidly prepared directly onto the photoelectrode surface without further thermal treatments. This attracting approach was recently exploited to carry out in situ X-ray absorption spectroscopy studies[27] because, thanks to the "full-mass" contact with the electrolyte (high hydration), all Ir sites participated to the electrochemical processes.[34] The onset potential of H2 was anticipated of about 200 mV by the presence of the IrO_x film (Figure 6b). The beneficial effect of IrO_x was pronounced at bias below +1.25 V_{RHE}, inducing a 385 and 250% photocurrent enhancement at +1.0 and +1.1 V_{RHE}, respectively. At more anodic applied bias, the curve of H2/IrO_x crossed the H2 one, showing a different trend than IrO_2 nanoparticles.[9]

In general, the effects of a surface layer can be multifaceted: on one side, it possibly acts as OER catalyst in speeding-up the reaction kinetics. This action reflects on a shift of the current onset at less positive potential.[9] On the other side, the catalyst can quench surface defects (recombination centers) and modify the space charge layer thus increasing the minority charge carrier lifetime.[35] In our case, we observed a beneficial effect of IrO_x in reducing the onset potential, while decreasing the photocurrent plateau. This behavior suggests that highly hydrated IrO_x layer can act as electrocatalyst but not as surface defects quencher.

CONCLUSIONS

Deposition of highly crystalline α-Fe_2O_3 nanostructures by single-step PE-CVD produced a novel nanoplatelets morphology. The growth of such films was directed by a multiple length scales organization into hierarchical plume-like nanoplatelets having nanobranches with dimension in the order 10 nm in width and 50 nm in length. The grown films had a strong preferential orientation of (001) crystallographic planes perpendicular to the conductive glass surface. The photoactivity of nanostructured films was crucially affected by both the platelets density and roughness. The best balance between platelets density and roughness (optimized semiconductor/water interface) resulted in the most performing photoanodes. At high precursor loading (H5), the photocurrent could be also influenced by the presence of high angle grain boundaries at the interface between the single nanobranches and small nanoparticles growing at their top. The α-Fe_2O_3 photoelectrodes showed promising PEC water splitting activities that are prone to further increase by optimization of synthetic procedures (i.e., by one-step doping).

Finally, reported results obtained by a simple deposition of highly hydrated IrO_x overlayer, revealed its beneficial effect in reducing the onset potential and witnessed how the nanoplatelets are a versatile building block suitable for the development of complex multilayer architectures.

ASSOCIATED CONTENT

Supporting Information

The scheme of PE-CVD apparatus, additional XRD, SEM, TEM, UV−vis, and table of both crystallite size and photocurrent densities. This material is available free of charge via the Internet at http://pubs.acs.org.

AUTHOR INFORMATION

Corresponding Authors

*E-mail: v.dalsanto@istm.cnr.it.
*E-mail: a.naldoni@istm.cnr.it

Author Contributions

‡These authors contributed equally.

Notes

The authors declare no competing financial interest.

ACKNOWLEDGMENTS

Financial support from the Italian Ministry of Education, University and research (MIUR) through the FIRB project "Low-cost photoelectrodes architectures based on the redox cascade principle for artificial photosynthesis" (RBFR13XLJ9), and from Regione Lombardia through the project "SOLAR ENERGY: technology and materials for the efficient use of solar energy" − Accordo Quadro Regione Lombardia − CNR is gratefully aknowledged.

REFERENCES

(1) Li, Z.; Luo, W.; Zhang, M.; Feng, J.; Zou, Z. Photoelectrochemical Cells for Solar Hydrogen Production: Current State of Promising Photoelectrodes, Methods to Improve Their Properties, and Outlook. *Energy Environ. Sci.* **2013**, *6*, 347−370.

(2) Lee, M. H.; Takei, K.; Zhang, J.; Kapadia, R.; Zheng, M.; Chen, Y.-Z.; Nah, J.; Matthews, T.; Chueh, Y.-L.; Ager, J. W.; Javey, A. p-Type InP Nanopillar Photocathodes for Efficient Solar-Driven Hydrogen Production. *Angew. Chem., Int. Ed.* **2012**, *51*, 10760−10764.

(3) Paracchino, A.; Mathews, N.; Hisatomi, T.; Stefik, M.; Tilley, S. D.; Grätzel, M. Ultrathin Films on Copper(I) Oxide Water Splitting

Photocathodes: a Study on Performance and Stability. *Energy Environ. Sci.* **2012**, *5*, 8673−8681.
(4) Chen, S.; Wang, L.-W. Thermodynamic Oxidation and Reduction Potentials of Photocatalytic Semiconductors in Aqueous Solution. *Chem. Mater.* **2012**, *24*, 3659−3666.
(5) Lin, Y.; Yuan, G.; Sheehan, S.; Zhou, S.; Wang, D. Hematite-Based Solar Water Splitting: Challenges and Opportunities. *Energy Environ. Sci.* **2011**, *4*, 4862−4869.
(6) Bora, D. K.; Braun, A.; Constable, E. In Rust We Trust". Hematite − the Prospective Inorganic Backbone for Artificial Photosynthesis. *Energy Environ. Sci.* **2013**, *6*, 407−425.
(7) Sivula, K.; Le Formal, F.; Grätzel, M. Solar Water Splitting: Progress Using Hematite (α-Fe_2O_3) Photoelectrodes. *ChemSusChem* **2011**, *4*, 432−449.
(8) Sivula, K.; Zboril, R.; Le Formal, F.; Robert, R.; Weidenkaff, A.; Tucek, J.; Frydrych, J.; Grätzel, M. Photoelectrochemical Water Splitting with Mesoporous Hematite Prepared by a Solution-Based Colloidal Approach. *J. Am. Chem. Soc.* **2010**, *132*, 7436−7444.
(9) Tilley, S. D.; Cornuz, M.; Sivula, K.; Grätzel, M. Light-Induced Water Splitting with Hematite: Improved Nanostructure and Iridium Oxide Catalysis. *Angew. Chem., Int. Ed.* **2010**, *49*, 6405−6408.
(10) Kay, A.; Cesar, I.; Grätzel, M. New Benchmark for Water Photooxidation by Nanostructured α-Fe_2O_3 Films. *J. Am. Chem. Soc.* **2006**, *128*, 15714−15721.
(11) Warren, S.; Voïtchovsky, K.; Dotan, H.; Leroy, C.; Cornuz, M.; Stellacci, F.; Hébert, C.; Rothschild, A.; Grätzel, M. Identifying Champion Nanostructures for Solar Water-Splitting. *Nat. Mater.* **2013**, *12*, 842−849.
(12) Deng, J.; Lv, X.; Gao, J.; Pu, A.; Li, M.; Sun, X.; Zhong, J. Facile Synthesis of Carbon-Coated Hematite Nanostructures for Solar Water Splitting. *Energy Environ. Sci.* **2013**, *6*, 1965−1970.
(13) Duret, A.; Grätzel, M. Visible Light-Induced Water Oxidation on Mesoscopic α-Fe_2O_3 Films Made by Ultrasonic Spray Pyrolysis. *J. Phys. Chem. B* **2005**, *109*, 17184−17191.
(14) Cesar, I.; Kay, A.; Gonzalez Martinez, J. A.; Grätzel, M. Translucent Thin Film Fe_2O_3 Photoanodes for Efficient Water Splitting by Sunlight: Nanostructure-Directing Effect of Si-Doping. *J. Am. Chem. Soc.* **2006**, *128*, 4582−4583.
(15) Bora, D. K.; Braun, A.; Erni, R.; Fortunato, G.; Graule, T.; Constable, E. C. Hydrothermal Treatment of a Hematite Film Leads to Highly Oriented Faceted Nanostructures with Enhanced Photocurrents. *Chem. Mater.* **2011**, *23*, 2051−2061.
(16) Kim, J. Y.; Magesh, G.; Youn, D. H.; Jang, J.-W.; Kubota, J.; Domen, K.; Lee, J. S. Single-crystalline, Wormlike Hematite Photoanodes for Efficient Solar Water Splitting. *Sci. Rep.* **2013**, *3*, 2681−2688.
(17) Mohapatra, K.; John, S. E.; Banerjee, S.; Misra, M. Water Photooxidation by Smooth and Ultrathin α-Fe_2O_3 Nanotube Arrays. *Chem. Mater.* **2009**, *21*, 3048−3055.
(18) Wang, G.; Ling, Y.; Wheeler, D. A.; George, K. E. N.; Horsley, K.; Heske, C.; Zhang, J. Z.; Li, Y. Facile Synthesis of Highly Photoactive α-Fe_2O_3-Based Films for Water Oxidation. *Nano Lett.* **2011**, *11*, 3503−3509.
(19) Li, L.; Yu, Y.; Meng, F.; Tan, Y.; Hamers, R. J.; Jin, S. Facile Solution Synthesis of α-$FeF_3{\cdot}3H_2O$ Nanowires and Their Conversion to α-Fe_2O_3 Nanowires for Photoelectrochemical Application. *Nano Lett.* **2012**, *12*, 724−731.
(20) Ling, Y.; Wang, G.; Reddy, J.; Wang, C.; Zhang, J. Z.; Li, Y. The Influence of Oxygen Content on the Thermal Activation of Hematite Nanowires. *Angew. Chem., Int. Ed.* **2012**, *51*, 4074−4079.
(21) Ling, Y. C.; Wang, G. M.; Wheeler, D. A.; Zhang, J. Z.; Li, Y. Sn-Doped Hematite Nanostructures for Photoelectrochemical Water Splitting. *Nano Lett.* **2011**, *11*, 2119−2125.
(22) Larson, R. B. *ACVD, General Structural Analysis System*; Los Alamos National Laboratory: Los Alamos, NM, 2004; p 86.
(23) McCarthy, G. J.; Welton, J. M. X-Ray Diffraction Data for SnO_2. An Illustration of the New Powder Data Evaluation Methods. *Powder Diffr.* **1989**, *4*, 156−159.
(24) Sawada, H. An Electron Density Residual Study of α-Ferric Oxide. *Mater. Res. Bull.* **1996**, *31*, 141−146.
(25) Ayache, J.; Beaunier, L.; Boumendil, J.; Ehret, G.; Laub, D. In *Sample Preparation Handbook for Transmission Electron Microscopy*; Anderson, R., Ed.; Springer: New York, 2010; Chapter 4, pp 153−228.
(26) Cabanillas-Gonzalez, J.; Virgili, T.; Lanzani, G.; Yeates, S.; Ariu, M.; Nelson, J.; Bradley, D. D. C. Photophysics of Charge Transfer in a Polyfluorene/Violanthrone Blend. *Phys. Rev. B* **2005**, *71*, 014211−1−8.
(27) Minguzzi, A.; Lugaresi, O.; Locatelli, C.; Rondinini, S.; D'Acapito, F.; Achilli, E.; Ghigna, P. Fixed Energy X-ray Absorption Voltammetry. *Anal. Chem.* **2013**, *85*, 7009−7013.
(28) Wen, X.; Wang, S.; Ding, Y.; Wang, Z. L.; Yang, S. Controlled Growth of Large-Area, Uniform, Vertically Aligned Arrays of α-Fe_2O_3 Nanobelts and Nanowires. *J. Phys. Chem. B* **2005**, *109*, 215−220.
(29) Dimitrijevic, N. M.; Savic, D.; Micic, O. I.; Nozik, A. J. Interfacial Electron-Transfer Equilibria and Flat-Band Potentials of α-Fe_2O_3 and TiO_2 Colloids Studied by Pulse Radiolysis. *J. Phys. Chem.* **1984**, *88*, 4278−4283.
(30) Harry, J. E. In *Introduction to Plasma Technology: Science, Engineering and Applications*; Hippler, R., Kersten, H., Schmidt, M., Schoenbach, K. H., Eds.; Wiley: Weinheim, Germany, 2010; Chapter 1, 3−13.
(31) Cherepy, N. J.; Liston, D. B.; Lovejoy, J. A.; Deng, H.; Zhang, J. Z. Ultrafast Studies of Photoexcited Electron Dynamics in γ- and α-Fe_2O_3 Semiconductor Nanoparticles. *J. Phys. Chem. B* **1998**, *102*, 770−776.
(32) Minguzzi, A.; Fan, F.-R. F.; Vertova, A.; Rondinini, S.; Bard, A. J. Dynamic Potential−pH Diagrams Application to Electrocatalysts for Water Oxidation. *Chem. Sci.* **2012**, *3*, 217−229.
(33) Steegstra, P.; Ahlberg, E. Involvement of Nanoparticles in the Electrodeposition of Hydrous Iridium Oxide Films. *Electrochim. Acta* **2012**, *68*, 206−213.
(34) Petit, M. A.; Plichon, V. Anodic Electrodeposition of Iridium Oxide Films. *J. Electroanal. Chem.* **1998**, *444*, 247−252.
(35) Barroso, M.; Mesa, C. A.; Pendlebury, S. R.; Cowan, A. J.; Hisatomi, T.; Sivula, K.; Grätzel, M.; Klug, D. R.; Durrant, J. R. Dynamics of Photogenerated Holes in Surface Modified α-Fe_2O_3 Photoanodes for Solar Water Splitting. *Proc. Natl. Acad. Sci. U.S.A.* **2012**, *109*, 15640−15640.